Direct numerical simulation of rotating fluid flow in a closed cylinder

Sørensen, Jens Nørkær; Christensen, Erik Adler

Published in:
Physics of Fluids

Link to article, DOI:
10.1063/1.868600

Publication date:
1995

Document Version
Publisher's PDF, also known as Version of record

Direct numerical simulation of rotating fluid flow in a closed cylinder

Jens Nørkær Sørensen[a)]
Department of Fluid Mechanics, Building 404, Technical University of Denmark, DK-2800 Lyngby, Denmark

Erik Adler Christensen
Institute of Mathematical Modelling, Building 305, Technical University of Denmark, DK-2800 Lyngby, Denmark

(Received 21 July 1994; accepted 27 December 1994)

Present numerical simulations of the transition scenario of a rotating fluid flow in a closed cylinder are presented, where the motion is created by a rotating lid. The numerical algorithm, which is based on a finite-difference discretization of the axisymmetric Navier-Stokes equations, is validated against experimental visualizations of both transient and stable periodic flows. The complexity of the flow problem is illuminated numerically by injecting flow tracers into the flow domain and following their evolution in time. The vortex dynamics appears as stretching, folding and squeezing of flow structures which wave along the contour of a central vortex core. The main purpose of the study is to clarify the mechanisms of the transition scenario and relate these to experiences known from other dynamical systems and bifurcation theory. The dynamical system was observed to exhibit up to three multiple solutions for the same Reynolds number, and to contain four discernible branches. The transition to strange attractor behavior was identified as a nontrivial Ruelle-Takens transition through a transient torus. The various solution branches of the rotating flow problem are illustrated by phase portraits and summarized on a frequency diagram. © *1995 American Institute of Physics.*

I. INTRODUCTION

In the last two decades a great number of investigations has been carried out to clarify the fundamental mechanisms of transitions in fluid dynamical systems. In general, these have focused on classical configurations of fluid flows, such as the Rayleigh-Bénard convection problem and the Taylor-Couette flow. Studies of these examples have revealed that the onset process is connected with a rich variety of flow phenomena. A breakthrough in understanding this was introduced by Ruelle and Takens,[1] who, under certain assumptions, proposed that if a dynamical system goes through a fourth Hopf-bifurcation at some critical number, then the system most probably becomes strange. Consequently, only three basic frequencies may appear in the power spectra simultaneously. When a fourth frequency is about to occur, the spectrum immediately becomes broadbanded with an overlaying spectral component, say R-T frequency. By a theorem of Plykin, Newhouse *et al.*[2] later proved that under further restrictions strange attractors may be obtained through only a third Hopf-bifurcation. Other important scenaria are due to Feigenbaum,[3] who connected the transition process to period doubling bifurcations, and to Pomeau and Manneville,[4] who identified four types of intermittency phenomena to be responsible for such transitions. Finally, Ostlund *et al.*[5] observed a phase-locking phenomenon connected with clumping and wrinkling of a torus, and Lorenz,[6] among others, observed an abrupt transition from steady to chaotic behavior as a subcritical Hopf-bifurcation. These different scenaria must be thought of as complementary, although multiple scenaria may coexist, as observed by e.g. Gollub and Benson.[7]

To analyze the transition scenario of rotating flows, we here consider a closed flow in a cylindrical container, where the rotation is initiated by a rotating lid. Letting dimensions be given by height, H, and radius, R, and assuming that one endwall rotates with angular velocity, Ω, see Fig. 1, the flow conditions are uniquely defined by the Reynolds number, $\mathrm{Re}=\Omega R^2/\nu$, where ν denotes the kinematic viscosity, the aspect ratio, $\lambda=H/R$, and some initial state. The physics of the flow may be summarized as follows:

With motion created by letting the one end cover rotate with a constant angular velocity, Ω, an Ekman layer of the thickness $O(\mathrm{Re}^{-1/2})$ is spontaneously built up through the action of viscous stresses.[8] Due to the no-slip condition, the flow, which adheres to the rotating endwall, is set into motion and centrifuged away towards the cylinder wall. The continuity of the incompressible fluid flow deflects the boundary layer downwards, forming a Stewartson layer at the side wall.[9] At the lower endwall, the boundary layer is bent, as a continuous layer, toward the center forming a lower Ekman layer. The no-slip condition now decelerates the fluid adjacent to the fixed endwall, which thus is exposed to a radial pressure gradient. The radial pressure gradient compensates for the centrifugal force acting on the rotating fluid in the inner part.[10] Consequently, the fluid inside the boundary layer converges towards the center axis, where it is sucked into the rotating center core, thus completing its path like a centrifugal pump.

The first study of this flow was carried out by Vogel,[11] who showed that for certain combinations of λ and Re, axisymmetric recirculation structures, interpreted as vortex breakdown, appeared near the center axis. Later, these visualizations were supplemented by laser-Doppler measurements for a flow with $\lambda=1.59$ and $\mathrm{Re}=1850$ by

a)e-mail: jns@afm.dtu.dk

 1070-6631/95/7(4)/764/15/$6.00

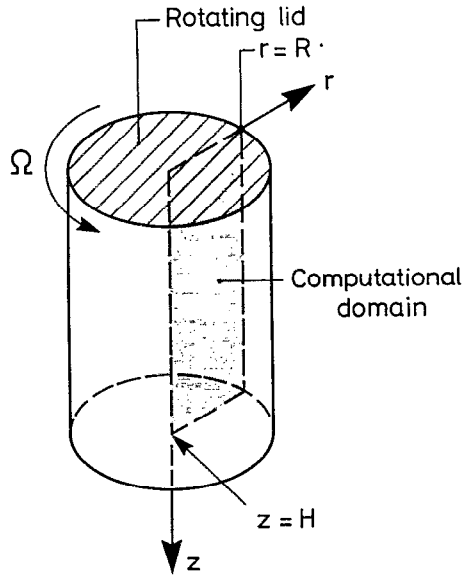

FIG. 1. Cylinder with rotating lid.

Ronnenberg.[12] To date, the most detailed experimental study has been carried out by Escudier,[13] see Fig. 2. Employing laser-induced fluorescence technique, Escudier showed that up to three distinct breakdown bubbles may occur, and by systematically changing the model parameters (λ,Re) he localized the domain of bubble regions and the limits of steady flow area. Later, LDA measurements has been performed by Michelsen,[14] and the PIV technique has been utilized by Westergaard *et al.*[15] in order to analyze unsteady flow structures. Recent experiments are due to Sørensen,[16] who performed a series of visualizations for the case of $\lambda=2$, and Spohn,[17] who studied also the case of a cylinder with a free surface.

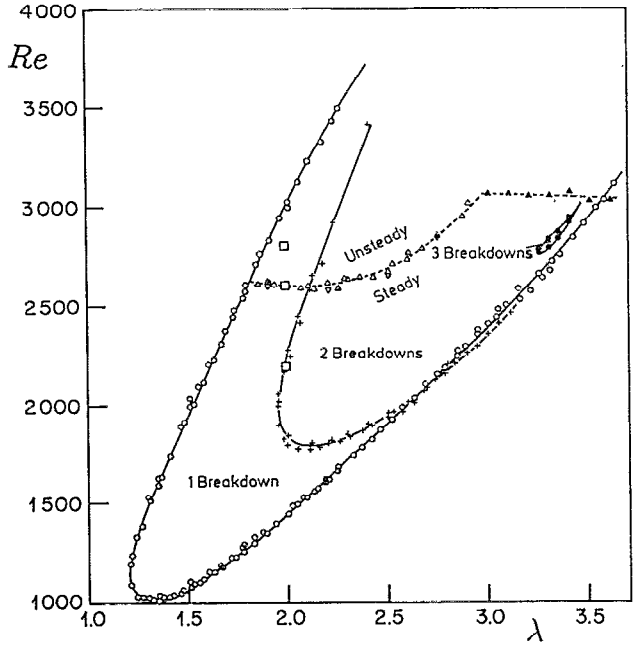

FIG. 2. Axisymmetric vortex breakdown by Escudier.[13] In present work, where $\lambda=2$, validation points are indicated by (□).

Owing to its simple geometry and the ease in establishing boundary conditions, the rotating cylinder flow has been the subject of a large number of numerical studies. Based upon solutions of the axisymmetric Navier-Stokes equations, results outside the parameter range where separation bubbles occur have been performed by e.g. Pao[18] and Bertela and Gori.[19] The first solutions showing the existence of separation bubbles are due to Lugt and Haussling.[20] These were later supplemented by Lugt and Abboud,[21] who systematically studied the influence of the model parameters by comparing their results to the visualizations of Escudier.[13] A similar investigation has recently been published by Lopez.[22] In general, the abovementioned calculations have focussed on investigation of the vortex breakdown up to the point where the flow becomes oscillatory. Solutions showing periodic oscillations have been found by Lopez,[23] Lopez and Perry,[24] and Daube and Sørensen,[25] revealing that the early transition is associated with several bifurcations, including period doubling phenomena. Recently, Christensen *et al.*[26] studied the early transition by applying a version of the Proper Orthogonal Decomposition technique.

The purpose of the present work is to analyze the numerical transition scenario of the flow from where it becomes oscillatory to where it breaks down to an aperiodic motion. The calculations are carried out employing a high-order, finite-difference approximation of the axisymmetric Navier-Stokes equations (Sørensen and Ta Phuoc[27]). We have limited ourselves only to treat the case of $\lambda=2$, and focussed on analyzing the influence of systematically changing the Reynolds number in the range from Re=500 to Re=8000.

II. FORMULATION OF PROBLEM

Assuming the fluid in the cylinder to have constant viscosity and density, up to symmetry breakdown the flow is governed by the axisymmetric and incompressible Navier-Stokes equations. These are here formulated in terms of vorticity, circulation and streamfunction (ω,Γ,ψ), with vorticity and circulation governed by transport equations and the streamfunction determined from a Poisson equation. The advantage of this formulation, as compared to the one of primitive variables, is that the pressure is eliminated and that continuity is automatically satisfied. Boundary conditions are established from the no-slip assumption of the velocity.

The solution of the resulting set of equations is accomplished by employing finite difference approximations in combination with ADI technique. The Poisson equation is solved with fourth order accuracy for the streamfunction utilizing a compact formulation based upon 3-point Hermitian formulas. To enhance the convergence rate the ADI algorithm is optimized by the relaxation procedure of Wachspress.[28] The transport equations are discretized by standard second-order differencing and solved by the ADI technique of Peaceman and Rachford.[29] The boundary conditions are implemented by either prescribing their values or

by making Taylor expansions from the boundary considered into the flow domain.

The solution is advanced in time as follows. First, the transport equations are solved for ω^n and Γ^n at time, $t=t^n$, with the streamfunction fixed at its value from the previous time, $\psi=\psi^{n-1}$. Next, the stream function, $\psi=\psi^n$, is determined from the Poisson equation with the vorticity, ω^n, given as a source term. Thus, in each time step the equations are solved decoupled. The time-discretization is related to the axial spacing, Δz, by $\Delta t=\alpha\Delta z$, where the constant α is limited by the CFL condition. It shall be noted that α is determined by the velocities of the secondary flow field, which are significantly smaller than the primary azimuthal velocity. Therefore, α may be given a greater value than the usual one of 0.5. By trying different values it was found that setting $\alpha=5$ in all cases resulted in stable solutions. Further details about the formulation and the numerical technique can be found in Sørensen and Ta Phuoc.[27]

III. VALIDATION OF THE NUMERICAL ALGORITHM

In earlier studies the employed numerical algorithm has been compared to steady measurements of the rotating driven cavity problem.[27] Here it was found that a grid of 71 radial nodes and 91 axial nodes was sufficient to resolve the flow field for the case of Re=1854 and $\lambda=2$. Furthermore, computed velocity distributions were in excellent agreement with the LDA measurements of Michelsen [14] for Re=1800 and $\lambda=1$. As the boundary layer at the rotating lid can be described as an Ekman layer with a thickness of the order $O(\mathrm{Re}^{-1/2})$, it is estimated that approximately twice as many mesh points are needed in each space direction when going from Re=1800 to Re=8000.

To test the influence of the grid resolution at higher Reynolds numbers three different grids consisting of respectively 80×160, 100×200, and 140×280 mesh cells were compared. The outcome of this study was that, except for a displacement of the values of the Reynolds number, the general behavior of the transition scenario did not depend critically on the grid resolution. Thus, they all exhibited both periodic, quasiperiodic and chaotic behavior, although a finer grid results in the transition to chaos being shifted to a higher Reynolds number. The test was carried out by comparing phase portraits and power spectra of time series of vorticity functions at points located centrally in the calculation domain. Here the chaotic behavior that was found to appear at Re=6900 on the coarse grid was similar to the chaotic behavior at Re=7500 on the next-coarse grid, and to about Re=8000 on the fine grid. These results evidence that the basic physical process determining the transition scenario is present over a wide range in mesh fineness. To find a compromise between accuracy and computing expenses it was decided to employ the next-coarse grid. Therefore, the results that will be presented in the next sections are all based on a resolution of 100×200 mesh cells.

To further validate the algorithm in the unsteady regime, results are compared to the visualizations of Sørensen.[16] These were performed by illuminating pine pollen suspended in a glycerin/water mixture by an oscillating laser beam. In contrast to the visualizations of Escudier,[13] where fluorescent dye was dissolved in the fluid, this technique does not contaminate the fluid and therefore makes it possible to study also the time-behavior of the flow. After a short time in the fluid the particles are nearly neutrally buoyant. However, due to the rotation of the fluid the particles do tend to migrate sideways. This results in a concentration difference between different regions of the flows, making structures such as vortical regions and secondary flow bubbles clearly visible. Numerically, the visualizations are performed by injecting particles around the axis near the fixed endwall and advecting them as passive flow tracers according to the particle equations,

$$\frac{dr_p}{dt}=u_p, \quad \frac{dz_p}{dt}=w_p, \tag{1}$$

where $[r_p(t),z_p(t)]$ denotes the position of the particle considered and $[u_p(t),w_p(t)]$ is the corresponding velocity vector. The equations are discretized by a simple explicit Adams-Bashforth approximation and solved along with the momentum equations.

The first part of the comparison was carried out by studying the transient behavior of the flow during the process of a sudden increase of the Reynolds number from 2200 to 2800. In Figs. 3(a)–3(d) we depict snapshots from video pictures at different times. At time $t=0$, Fig. 3(a), the flow is steady and two recirculating bubbles are observed to appear near the axis. After the Reynolds number has been changed

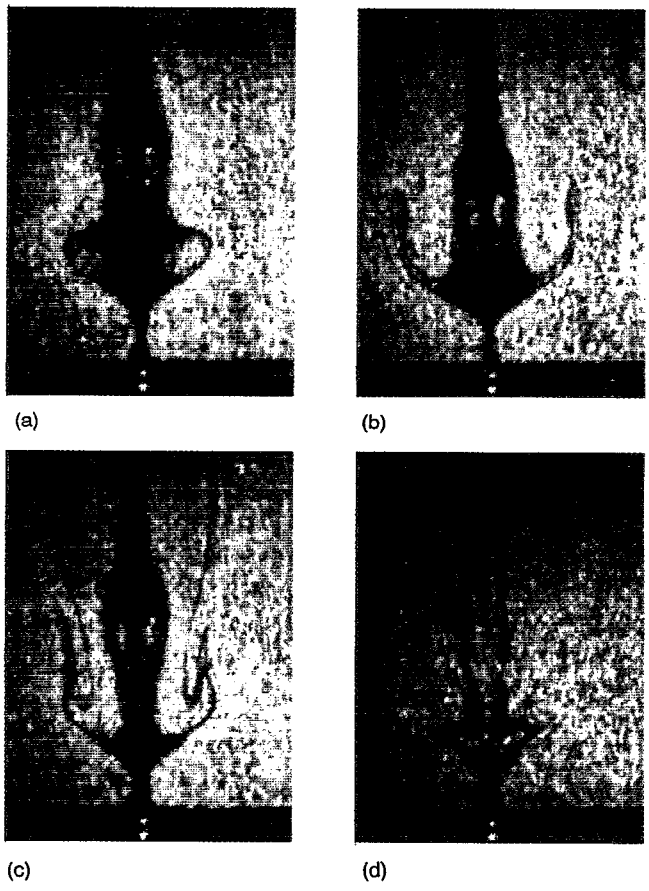

FIG. 3. (a)–(d) Visualizations of transient behavior due to a sudden increase from Re=2200 to Re=2800.

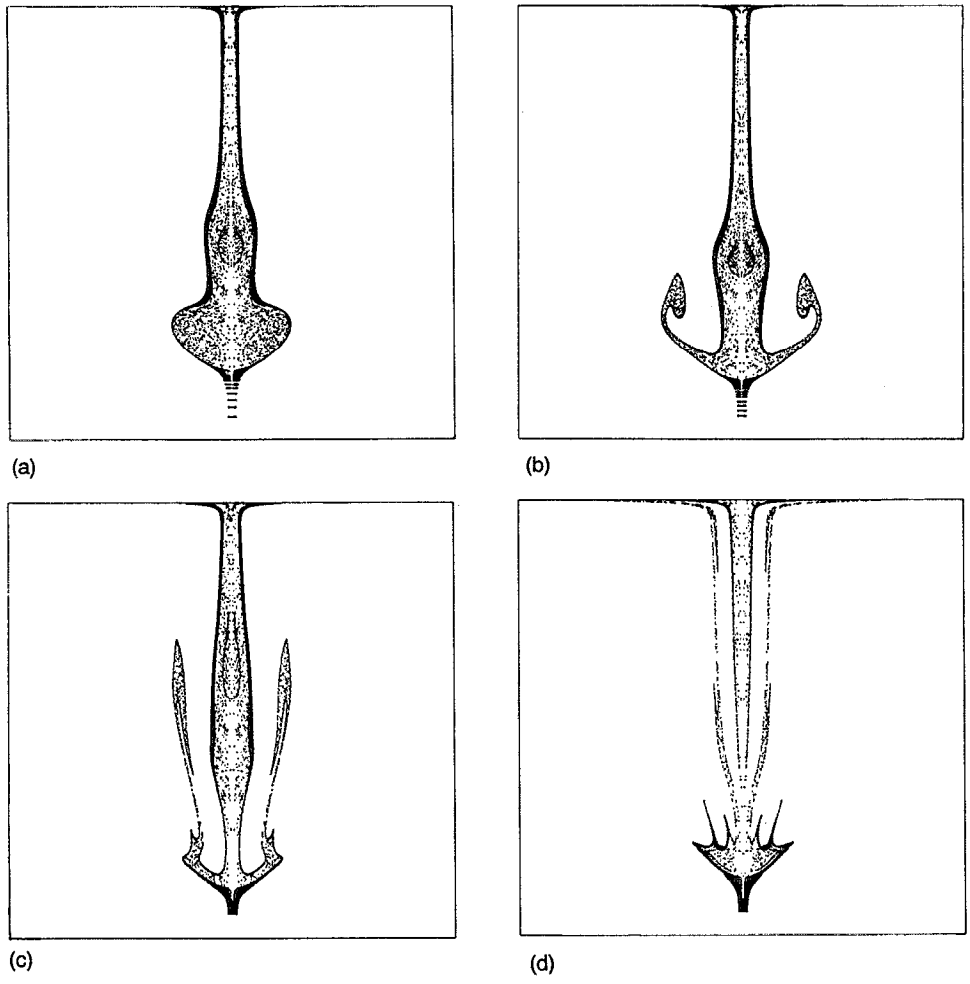

FIG. 4. (a)–(d) Numerical visualizations of transient behavior. Compare to Fig. 3.

to Re=2800, by increasing the frequency of the lid, we observe the development of a complex transient process. From the initial steady state the lower bubble expands and becomes more edge-formed. At about $t=50$ the breakdown bubble takes a deep breath downwards, with the edge being stretched upwards following the secondary meridional flow. Consequently, two fingers on the cross section are developed, see Fig. 3(b). Next, the lower bubble shrinks at the same time as the fingers are prolonged further towards the rotating lid. Then the lower section almost instantaneously pumps down, and decouples from the upper breakdown bubble. On their return, Fig. 3(c), the fingers finally fold. This process continues very regularly from hereon, where each pump movement results in the generation of new fingers. The eyes of the upper bubble are stretched and sucked towards the rotating lid, to finally disappear at about $t=200$. After several time periods the core attains a typical shape for Re=2800, as displayed in Fig. 3(d). It is noticed that the fingers produced by the periodic oscillations move along the contour as wave-trains, to be attached by the rotating lid. The corresponding numerical visualizations are shown in Figs. 4(a)–4(d). Although the structures in the experiment are due to particle depletion and the calculated structures are formed by injection of particles, the calculations are generally in good agreement with the experimental visualizations. It should also be noted that the structures in the experiment are stretched radially because of refraction. The second part of the validation was carried out for a stable periodic flow situation with Re = 2600, where experimental visualizations are presented in Figs. 5(a)–5(d). The periodic flow pattern is similar to the one just described, thus fingers are produced by stretching and folding mechanisms, implied by the periodic pumping process. This pattern is well reproduced by the numerical simulations, as seen in Figs. 6(a)–6(d). Particularly, the dynamic deformation of the edge and the occurrence of the wave-train along the core show that the calculations are in excellent agreement with the experiments. In accordance with the experiments of Escudier[13] we also find that the flow contains two breakdown bubbles at Re=2200 and that it is unsteady with one bubble at Re=2600 and Re=2800, as indicated in Fig. 2. In the experiments[16] it was found that the oscillating bubble structures disappear at Re≃3000 and instead a slender vortex subject to moving wave-trains is formed. Therefore, it is difficult to compare calculations to visualizations at higher Reynolds numbers. Furthermore, the vortex is found to perform a spiraling motion at about Re=3500, thus suggesting that the hypothesis of axial symmetry breaks down for Reynolds numbers greater than this value.

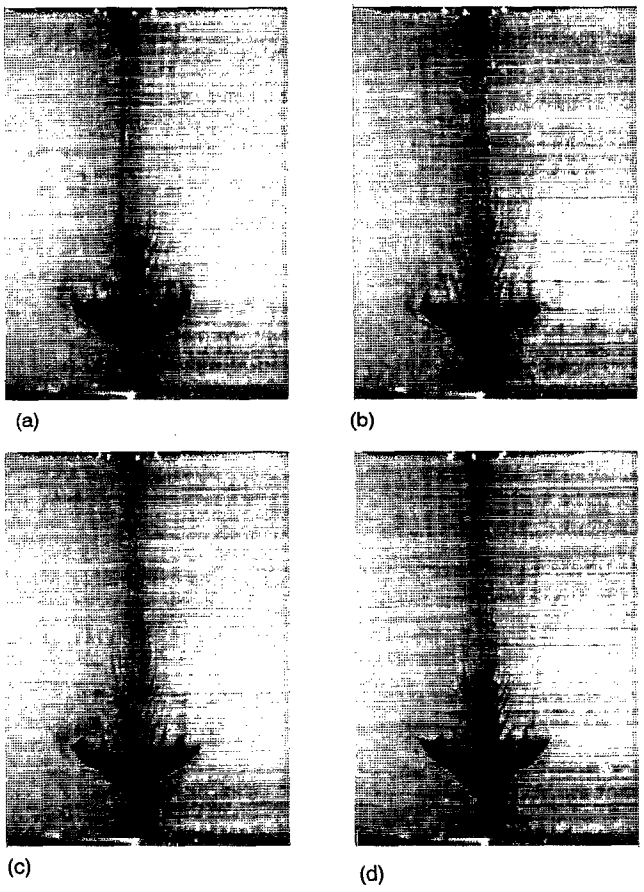

FIG. 5. (a)–(d) Visualizations of vortex formation for Re=2600. The periodic mechanism is most easily observed by following the formation of the outer edge in time.

IV. RESULTS

Although the visualizations indicate that axial symmetry, for Reynolds numbers higher than about 3500, breaks down to three-dimensional flow, the axisymmetric Navier-Stokes code may still unveil basic features of the transition process. In all cases, the axisymmetric solutions determine a unique scenario which in fact is equivalent to the three-dimensional scenario up to a certain critical Reynolds number.

A. Spatial flow structures

In the diagram of Escudier, Fig. 2, it is seen that up to two breakdown bubbles may be present in the $\lambda=2$ case. In agreement with the diagram, we find the first bubble to appear at about Re=1450 and two distinct bubbles in the range from Re=1800 to Re=2300. These bubbles are most easily recognized by plotting isolines of the streamfunction. When the flow becomes unsteady, however, a streamline plot gives an instantaneous picture of the flow pattern that is different from what is observed from releasing dye or particles into the fluid. Consequently, to analyze flow structures as they would be seen from experiments, one must resort to a Lagrangian description by injecting flow tracers into the fluid. In a recent study,[24] such a technique was utilized in combination with the KAM (Kolmogorov-Arnol'd-Moser) theory[30] to study the filling and emptying process of the vortex breakdown bubbles in a flow configuration with aspect ratio $\lambda=2.5$. Here a similar technique is employed by injecting particles around the center axis near the fixed endwall. These are subsequently advected as passive flow tracers according to the particle equations introduced in the previous section. Referring again to Figs. 6(a)–6(d), it is shown how streaklines from the injected particles at Re=2600 form the contour of an oscillating bubble structure. At this Reynolds number the flow is periodic with a basic frequency $f=0.24$, corresponding to a time period, $T=2\pi/f\simeq 26$. In the figures, snapshots are depicted almost equidistantly during one time-period. At the same time as it oscillates up and down, the bubble structure is seen to be dominated by axial fingers, generated by folding, stretching and squeezing of the outer edge of the bubble. Similar patterns were observed in the visualizations of Lopez and Perry.[24] From Fig. 2 it is shown that no vortex breakdown bubbles are present for Reynolds numbers greater than 3000. A similar behavior is found from the numerical visualizations. In Figs. 7(a)–7(c) snapshots from computed streaklines are depicted at Re=3000, 5000, and 7000, respectively. It is here seen that the oscillating bubble structure disappears and instead a slender vortex subject to moving wave-trains is formed. At Re=3000 the contour of a small bubble is still visible, whereas the structure at Re=5000 is dominated by small drop-shaped waves. Increasing further the Reynolds number, the drop-shaped structures become more thorny as shown in Fig. 7(c). For comparison, snapshots of isolines of the instantaneous streamfunction are shown in Figs. 8(a)–8(c). Here there is no evidence of the former observed vortex structures, instead the streamlines form recirculating bubbles of much larger length scales. By following the bubbles in time (not shown here) it was observed that they sometimes disappeared to be born again, and at other times up to three bubbles were visible. At Re=7000 recirculating bubbles furthermore appeared in the boundary layer of the sidewalls. The main effect of increasing the Reynolds number is that the topology of the streamlines becomes more complicated, thus at Re=7000 small bubbles are formed in the interior of the large structures.

B. Transition scenario

A detailed numerical analysis of the rotating flow problem has been performed by considering *stable* time series, where stability was assured by studying if trajectories of the transients were attracted or expelled from a given solution. By that, all final states, which do not diverge, may subsequently be taken as stable solutions. Now, parametrizing the meridional plane by coordinates, (i,j), where $z=(i-1)\Delta z$, and $r=(j-1)\Delta r$, time series of the vorticity function were taken at the following calculation points:

$$\mathcal{T}=\{(50,25),(50,75),(100,50),(150,25),(150,75)\}. \quad (2)$$

Since the geometry of the cylinder constitutes a closed flow system, it is absolutely unstable in the sense that the global dynamics is accessible from any point in the flow domain (see e.g. Huerre and Monkewitz[31]). Therefore, the vorticity functions selected are representative to the dynamics observed. The characteristics of the stable solutions considered were carefully identified by applying Fourier transforms,

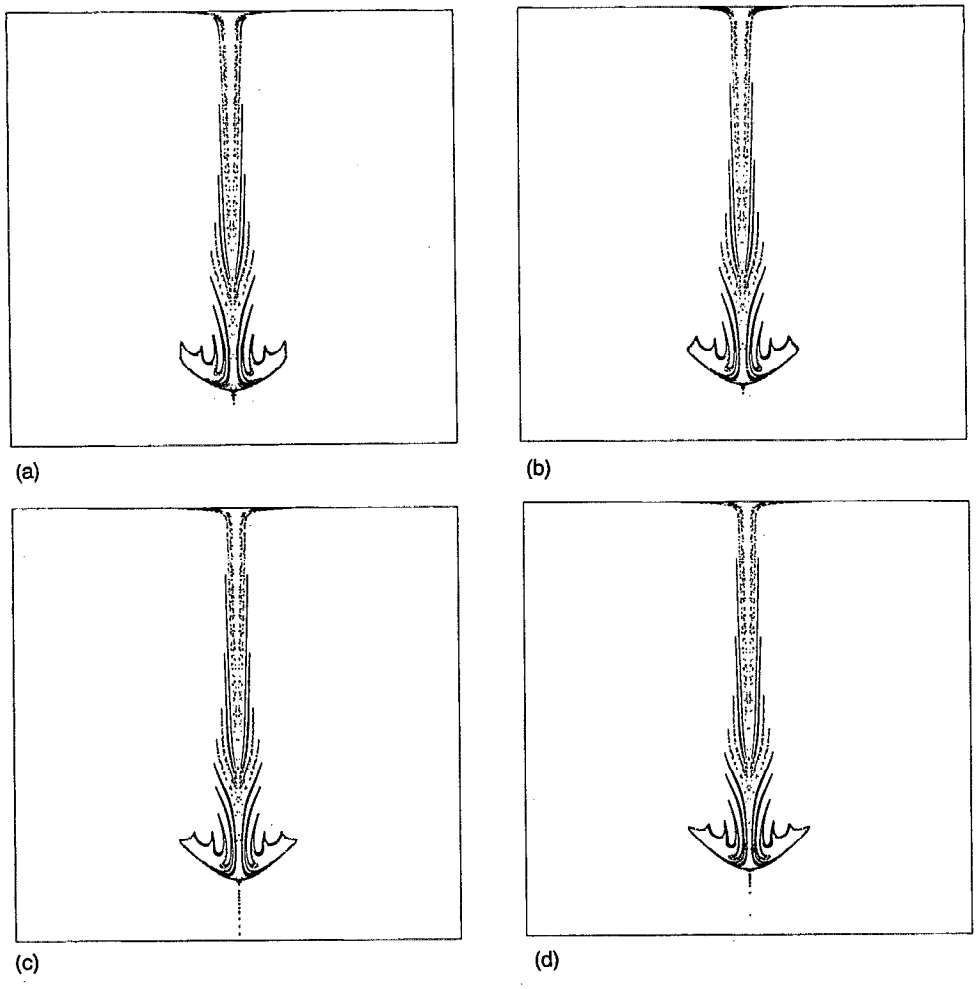

FIG. 6. (a)–(d) Numerical simulations of vortex formation for Re=2600, depicted almost equidistantly during one time-period. Compare to Fig. 5.

phase portraits, and Poincaré sections. Furthermore, to distinguish between deterministic chaos and random noise, correlation dimensions were calculated in the chaotic regime (see e.g. Grassberger and Procaccia[32] or Eckmann and Ruelle[33]). Denoting the time series in Eq. (2) by vort1 to vort5, the Fourier transforms were based on the sum over $\mathscr{F}$, i.e. vort1+...+vort5, and phase portraits by vort2(t) versus vort1(t), with time, t, as an internal parameter. In fact, any combination is possible, but this choice was found to represent the most clear picture of the transition process. The Poincaré sections are represented as the intersection between the hypersurface vort2(t_p)=constant, with constant chosen appropriately, and the phase portraits of [vort1(t),vort2(t),vort3(t)]. Mostly, however, fundamental changes in the transition process were unveiled from shifts in basic frequencies of the Fourier transforms and compared to corresponding phase portraits. This leads to the transition scenario presented in Fig. 9, where basic frequencies are

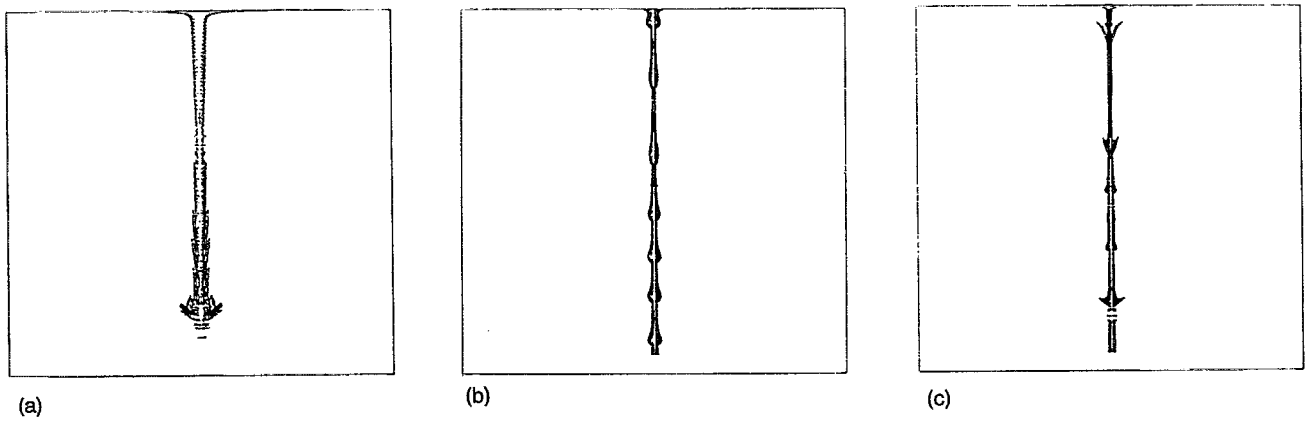

FIG. 7. (a)–(c) Vortex cores for Re=3000, 5000, 7000.

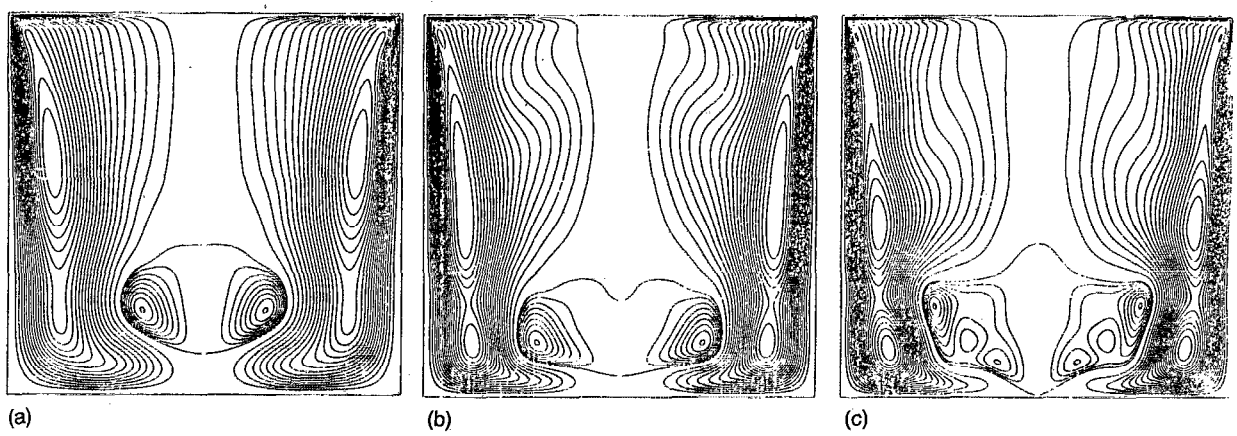

FIG. 8. (a)–(c) Breakdown bubbles for Re=3000, 5000, 7000.

shown as functions of the Reynolds number. Note that the harmonics of the Fourier components only state the degeneracy, and thus give no qualitative information about the transition process. Certainly, an inverse period doubling transfers energy from odd to the even spectral components, but this just appears as a change in the basic frequency. As no external forced frequency is present, the system is unlocked, and frequencies are allowed to change continuously between transitions.

The Reynolds numbers for the numerical simulations have been changed sequentially. Assuming that a stable solution exists at some Re_0, we wish to analyze how this develops as function of Re by finding the branch that generates from Re_0. As a first step we select a value, Re_1, some distance away from Re_0, and identify the corresponding stable solution. If the phase portrait at Re_0 looks similar to the one at Re_1, they are said to be connected by a branch on the (f,Re)-diagram, and the analysis is further proceeded from hereon. Otherwise, a new Re_1' is chosen by bisection and the corresponding stable solution found. The process continues until a one-way path between two consecutive stable solutions may be explained by either a continuous deformation or by a bifurcation, justified by considering the corresponding phase portraits. A branch is defined as a continuum of such similar solutions, starting and ending by a jump of hysteresis. Stable solutions apart from the branch analyzed thus indicate the existence of multiple solutions. When necessary, continuous variations of the branches were considered in both directions.

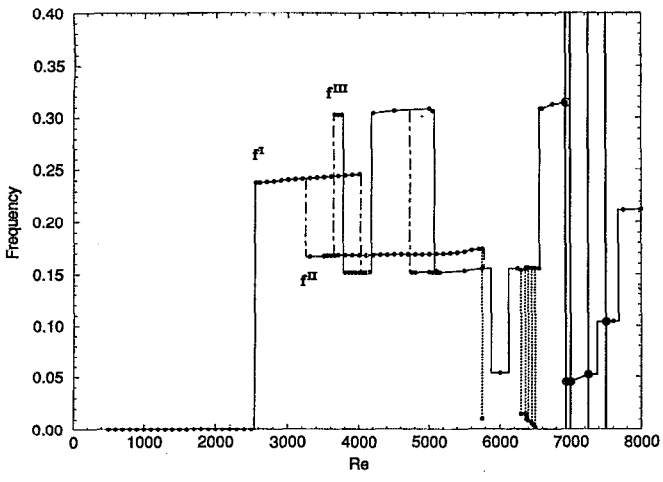

FIG. 9. Scenario of the rotating driven cavity problem. Stable solution (●); branch (—); hysteresis (---); stable R-T frequency (●); unstable R-T frequency (○); torus (···); chaos (—).

In Fig. 9 the branches are represented by (horizontal) solid curves connecting corresponding stable points. The branches are terminated by jumps of *hysteresis*, marked at both endpoints by vertical dash–dotted lines. An *unstable R-T frequency* means that a transient spectral component (R-T frequency), which originates from a Ruelle-Takens transition, has been observed to go through an unstable torus. A *stable R-T frequency*, on the other hand, means that a spectral component remains after the appearance of a broadband structure. A *torus* needs two basic frequencies, and is thus marked by a vertical dotted line connecting these, whereas a *chaotic* solution is defined by a continuous (nondiscrete) spectrum and therefore is illustrated by a vertical solid line.

The consumption in CPU-time on the vector processor Amdahl VP1200 amounts typically to about 15 CPU-minutes for a stationary solution, 2–6 CPU-hours for a periodic solution close to a critical point, and 10–20 CPU-hours near the onset point where the solutions become strange. This consumption is reduced if an initial solution is close to a target solution, and increased when critical points are approached.

In Table I the observed behavior of the basic frequencies has been related to concepts known from bifurcation theory. In the table superscripts, +, −, denote the limits of a basic frequency, f, decreasing from above, respectively increasing from below some given Reynolds number, Re. Typically, a continuity point, $f(\mathrm{Re}^+)=f(\mathrm{Re}^-)$, reflects a continuous deformation and therefore no transition is expected here, whereas a discontinuity point, $f(\mathrm{Re}^+)\neq f(\mathrm{Re}^-)$, indicates that some kind of transition has taken place. No rules from the theory of torus bifurcations have been introduced, except that both frequencies may vary continuously as function of Re. It therefore may appear that the two frequencies incidentally become rational dependent, thus suggesting a periodic

TABLE I. Transitions related to basic frequencies.

Change of $f(\mathrm{Re})$ with Re	Fundamental transition
Continuous change	No transition.
$f(\mathrm{Re}^+) \neq 0$, $f(\mathrm{Re}^-)=0$	Stationary to periodic solutions, Hopf-bifurcation.
$f(\mathrm{Re}^+)=1/n \cdot f(\mathrm{Re}^-)$	An n-period doubling bifurcation, ($n=2$ is simply a period doubling).
$f(\mathrm{Re}^+)=n \cdot f(\mathrm{Re}^-)$:	An inverse n-period doubling bifurcation.
$f_1(\mathrm{Re}^+)=f_1(\mathrm{Re}^-)$,	Periodic to quasiperiodic transition.
$f_2(\mathrm{Re}^+) \neq 0$, $f_2(\mathrm{Re}^-)=0$	Hopf-bifurcation.
$f(\mathrm{Re}^+) \neq pf(\mathrm{Re}^-)$ and $\neq 1/q \cdot f(\mathrm{Re}^-)$ for $\forall p,q \in \mathcal{N}$	Hysteresis.
$f_1(\mathrm{Re})/f_2(\mathrm{Re}) \in \mathcal{Q}$	Asymptotic quasiperiodic solution on a torus.

solution, which in fact is an asymptotic quasiperiodic solution on a torus.[34]

Table I was applied to identify all the bifurcations of the transition scenario. A full description is summarized in Table II. Subscripts '1' and '2' have been introduced in order to distinguish between the two frequencies that define a torus. Furthermore, we have introduced the fundamental frequencies, f^I, f^{II}, and f^{III}, which are maintained through the bifurcations. They are assumed to be fundamental to the system, because they are almost constant as Re is varied. In the following, the calculated solution branches will be presented and their properties discussed.

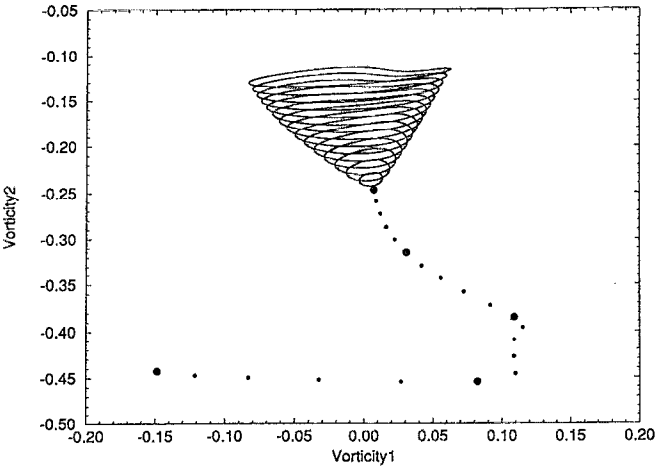

FIG. 10. Branch of early transition. Stationary solutions (·); Re=500, 1000, 1500, 2000, 2500 (●); periodic orbits (—).

The branch of early transition, 0≤Re≤4000: This branch determines the early part of the transition scenario, that goes from the steady to the periodic regime. In Fig. 10 phase portraits are presented at equidistantly distributed Reynolds numbers in the range from Re=500 to Re=4000, with an increment ΔRe=100. The enlarged dots denote stationary solutions at respectively Re=500, 1000, 1500, 2000, and 2500. As can be seen by the continuation of the path formed

TABLE II. Branches of the transition scenario.

Re	Fundamental transition
Branch of early transition, 0≤Re≤4000.	
– 1500,1750	Stationary bifurcations, 1st and 2nd vortex breakdown.[13]
– 2544	Supercritical Hopf-bifurcation.
– 4000–4050	Hysteresis.
Branch through hysteresis, 3300≤Re≤5750.	
– 3200–3300	Hysteresis.
– 5700–5750	Hopf-bifurcation to a torus.
– 5750–5800	Hysteresis.
Branch of hysteresis, 3650≤Re≤5100.	
– 3625–3650	Hysteresis.
– 3750–3800	Period doubling.
– 4150–4200	Inverse period doubling.
– 5050–5100	Period doubling.
– 5100–5125	Hysteresis to equal frequency.
Branch of onset, 4750≤Re≤8000.	
– 4700–4750	Hysteresis.
– 5750–6000	3-period doubling.
– 6000–6250	Inverse 3-period doubling.
– 6250–6300	Hopf-bifurcation to a torus. Continuous decay of secondary frequency.
– 6500–6551	No identified transition to a periodic solution.
– 6551–6580	Inverse period doubling.
– 6939	R-T transition to strange attractor through an unstable torus. The appeared frequency maintained.
– 7250–7500	Inverse period doubling of underlying attractor.
– 7500–7520	R-T transition from strange attractor to periodic solution.
– 7600–7750	Inverse period doubling.

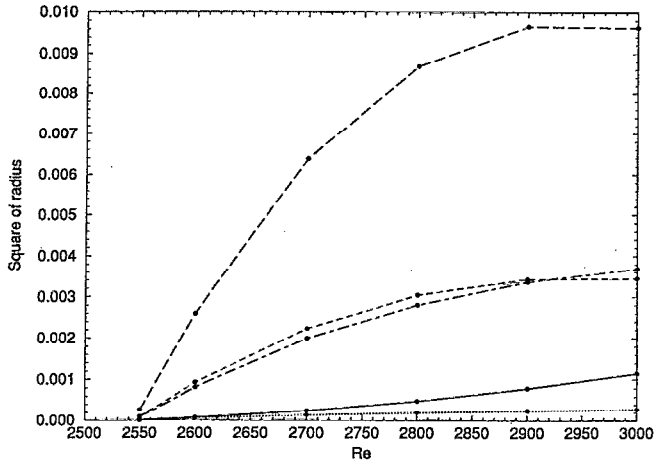

FIG. 11. Re_{Cr} estimated by extrapolation from time series. Vort1 (—); Vort2 (···); Vort3 (----); Vort4 (–––); Vort5 (–·–·).

by the dots, the vortex breakdown occurring at Re=1500 apparently does not affect the position of the stationary part of this branch. The transition from steady to periodic flow is typically associated with a Hopf-bifurcation at some critical Reynolds number, Re_{Cr}, where the stationary solution turns unstable. In Fig. 10 the Hopf-bifurcation looks supercritical, which can be verified by considering the expansion of the circular orbits into the unsteady domain. Denoting by R the radii of these orbits, a supercritical Hopf-bifurcation is approximated by

$$R \propto \sqrt{(\mathrm{Re}-\mathrm{Re}_{Cr})} + O(\mathrm{Re}-\mathrm{Re}_{Cr}). \tag{3}$$

In Fig. 11 the square of the radius of the five time series, vort1,...,vort5, is plotted against Re. The fact that the curves go through the same point and become linear near this, verifies that the transition to periodic flow is governed by a supercritical Hopf-bifurcation. The intersection of the curves shows a critical Reynolds number of $Re_{Cr}=2540$. This may be compared to the (λ,Re) diagram by Escudier, Fig. 2,

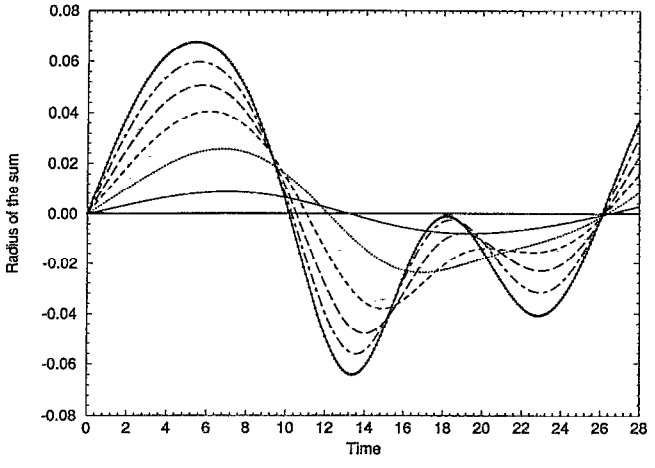

FIG. 12. Increasing domination of harmonic components in time series. Re=2500 (—); Re=2550 (—); Re=2600 (···); Re=2700 (----); Re=2800 (–––); Re=2900 (----); Re=3000 (•–•).

where oscillations set in at about Re=2550 for $\lambda=2$. Another property of the bifurcation is illustrated in Fig. 12, where we have plotted time series at Re=2500, 2550,..., 3000. In the figure these are denoted as radius of the sum and were constructed by taking the sum of vort1,..., vort5 and subtracing the mean value. The phase delays were eliminated simply by displacing the curves to a common origin. For Re=2550 the time series looks almost sinusoidal, in agreement with the assumption of a supercritical Hopf-bifurcation. As the Reynolds number is increased further harmonics are seen to be formed. Considering again the transition scenario, Fig. 9, the basic frequency at Re=2550 is $f=0.238$, corresponding to a period, $T\simeq 26$. This also defines the first fundamental frequency, f^I. Note that the period of one revolution of the lid is given as $T_{lid}=2\pi$ (dimensionless) seconds. The basic frequency increases linearly up to Re=4000, where it attains a value $f^I=0.246$. The linear dependence of the frequency on the distance to a critical number is a third well-known feature of the Hopf-bifurcation. At Re=4000 the rate of attraction was observed to be vanishing, which means that the time of convergency goes to infinity. Denoting the most critical multiplier[35] of the periodic solution by γ_1, the time of convergency goes approximately as

$$T_\infty = T\,\frac{1}{ln(1/\|\gamma_1\|)}\,ln(R_0/R_\infty). \tag{4}$$

T denotes the period of the stable periodic solution, and T_∞ the time of convergency to enter from a tube with radius R_0, into a tube with radius R_∞. Specifically, approaching a critical Reynolds number, Re_{Cr},

$$\|\gamma_1(\mathrm{Re})\| \to 1 \text{ for } \mathrm{Re}\to\mathrm{Re}_{Cr} \Rightarrow T_\infty \to \infty \text{ for } \mathrm{Re}\to\mathrm{Re}_{Cr}. \tag{5}$$

Therefore the branch is assumed to approach a critical point at Re=4000, which most probably is a saddle-node bifurcation point.

The branch through hysteresis, 3300≤Re≤5750: This branch proceeds through the domain of hysteresis by a continuous deformation of the solutions and ends, just before hysteresis, by a second Hopf-bifurcation to a torus. The frequency, which now is denoted as the second fundamental frequency, changes only slightly from $f^{II}=0.167$ at Re=3300 to $f^{II}=0.174$ at Re=5700. At Re=5750 a Hopf bifurcation introduces a secondary frequency $f_2^{II}=0.0109$. This is demonstrated in Figs. 13(a)–13(f), which shows a continuous deformation from Re=4000 to Re=5600, and, caused by the Hopf-bifurcation, a quasiperiodic solution at Re=5750. In Fig. 13(b) a cusp occurs on the phase portrait. This does not, however, give rise to a singularity point. In fact, the adding of a further phase dimension will smooth the curve. When decreasing the Reynolds number from 3300 to 3200 the rate of convergence became significantly slow, with the solution finally being attracted towards another stable branch. Therefore, a second saddle-node point might be assumed here. A saddle-node bifurcation is characterized by the collapsing of a stable and an unstable branch, which both exist at only one side of Re. Thus, a likely explanation for

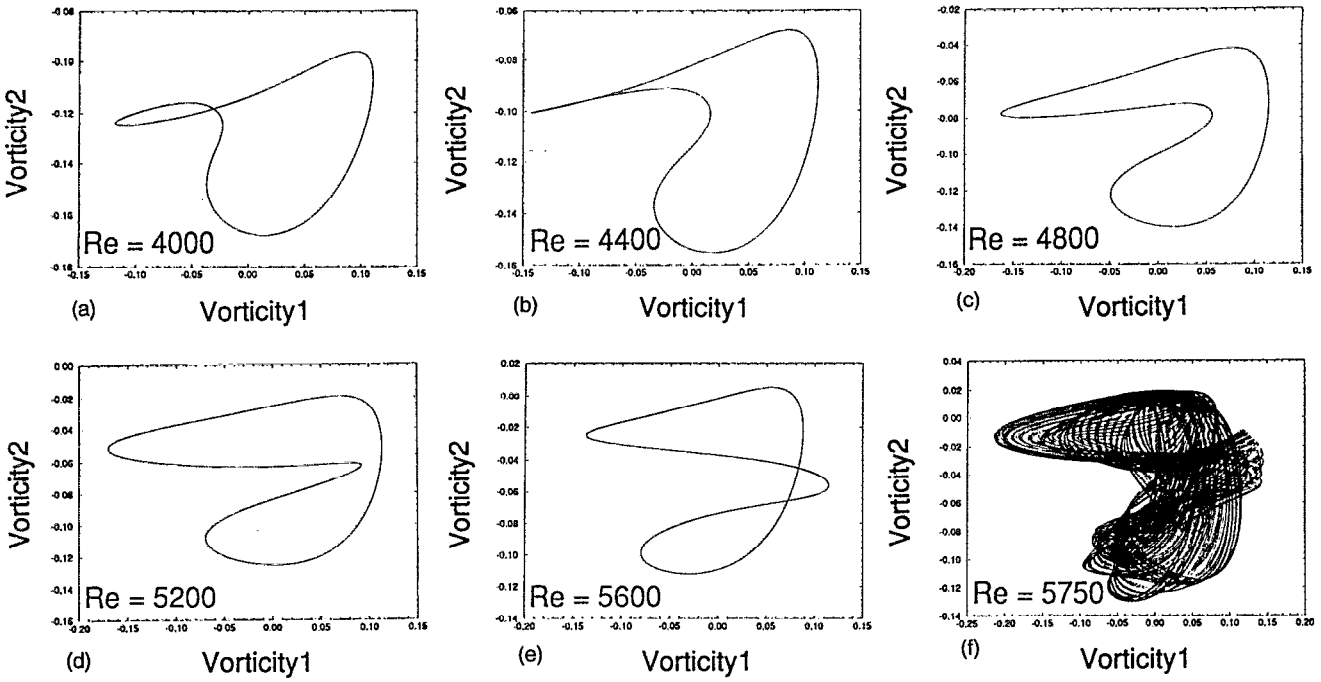

FIG. 13. (a)–(f) Branch through hysteresis by phase portraits.

the first hysteresis observed, is that the two branches are connected by an *unstable branch of hysteresis* through the saddle-node points.

The branch of hysteresis, 3650≤Re≤5100: This branch goes through three bifurcations, alternating between comparable parts of the branch. The branch introduces the third fundamental frequency, f^{III}, see Fig. 9. At the beginning and the end of the branch the rate of attraction was observed to be relatively high, thus no pitchfork, transcritical, or saddle-node bifurcations are expected here. In the range from Re=3650 to Re=3750, the frequency is fixed at a value $f^{III}=0.303$. This bifurcates by a period doubling to $f=1/2f^{III}=0.156$ at Re=3800. Note that $f(\mathrm{Re}^{+})=1/2f^{III}(\mathrm{Re}^{-})$, as stressed in Table I. Following the branch, the solution bifurcates by an inverse period doubling from $f=0.152$ at Re=4150 to $f^{III}=0.304$ at Re=4200. A last period doubling is obtained from $f^{III}=0.307$ at Re=5050 to $f=1/2f^{III}=0.153$ at Re=5100, and a small further increase in the Reynolds number results in a momentary change of branches. The phase portraits are nonsimilar, whereas the frequencies are almost equal. In Figs. 14(a)–14(f), the route of hysteresis is shown by representing various parts of the branch by phase portraits. Note the similarity of, for example, Figs. 14(a) and 14(d).

The branch of onset, 4750≤Re≤8000: This last branch contains all the non-trivial bifurcations. Entering from the *branch of hysteresis* at Re=5100, the phase portraits changed momentarily, while the frequencies remained nearly constant. Following the *branch of onset*, small steps in the Reynolds number had to be taken in order to pass the *branch of hysteresis* at Re=5100, otherwise the solution would change branch. Consequently, we may conclude that the two basins of attraction come very close at certain points. Following the *branch of onset* from the starting point, $f=1/2f^{III}=0.152$ at Re=4750, we pass the entering point at Re=5100 and meet a sequence consisting of a 3-periodic doubling from $f^{III}=0.155$ at Re=5750, to $f=1/6f^{III}=0.0537$ at Re=6000 and back again to $f^{III}=0.155$ at Re=6250, see Fig. 15(a)–15(c). At Re=6300, a second supercritical Hopf-bifurcation occurs with frequencies $f_1=1/2f^{III}=0.155$, and $f_2=0.0154$, thus introducing the domain of torii. This is seen in Figs. 15(d)–15(f). Coming from a periodic solution, Fig. 15(c), which turns 2-periodic by a second supercritical Hopf-bifurcation, we obtain the phase portrait shown in Fig. 15(d), or, after an expansion of the initial torus has taken place, to the one shown in Fig. 15(e). Note that the torii at Re=6300 and Re=6360 are similar except for a continuous expansion. The second frequency, f_2, is observed to decay dramatically, albeit continuously, through the quasiperiodic domain to become very small at Re=6500, where $f_1=0.156$ and $f_2=0.00258$. In the domain of torii, no hysteresis and no bifurcations have been observed. The torus in Fig. 15(f) looks distorted, but caused by the high ratio between the frequencies, it was impossible to produce a covering surface graphically. A final bifurcation, completing the domain of quasi-periodic solutions, has not been recognized as precisely as at the starting point, but it is assumed to be a subcritical Hopf-bifurcation, since the solutions turn from being quasiperiodic to periodic. Before the onset to the chaotic region, we met an inverse period doubling from $f=1/2f^{III}=0.156$ at Re=6551 to $f^{III}=0.309$ at Re=6580, and the onset scenario to chaotic solutions by a Ruelle-Takens scenario at Re=6939. Here, the power spectrum turns broad-banded with a single energetic spectral component, called a R-T frequency. The component is not identical

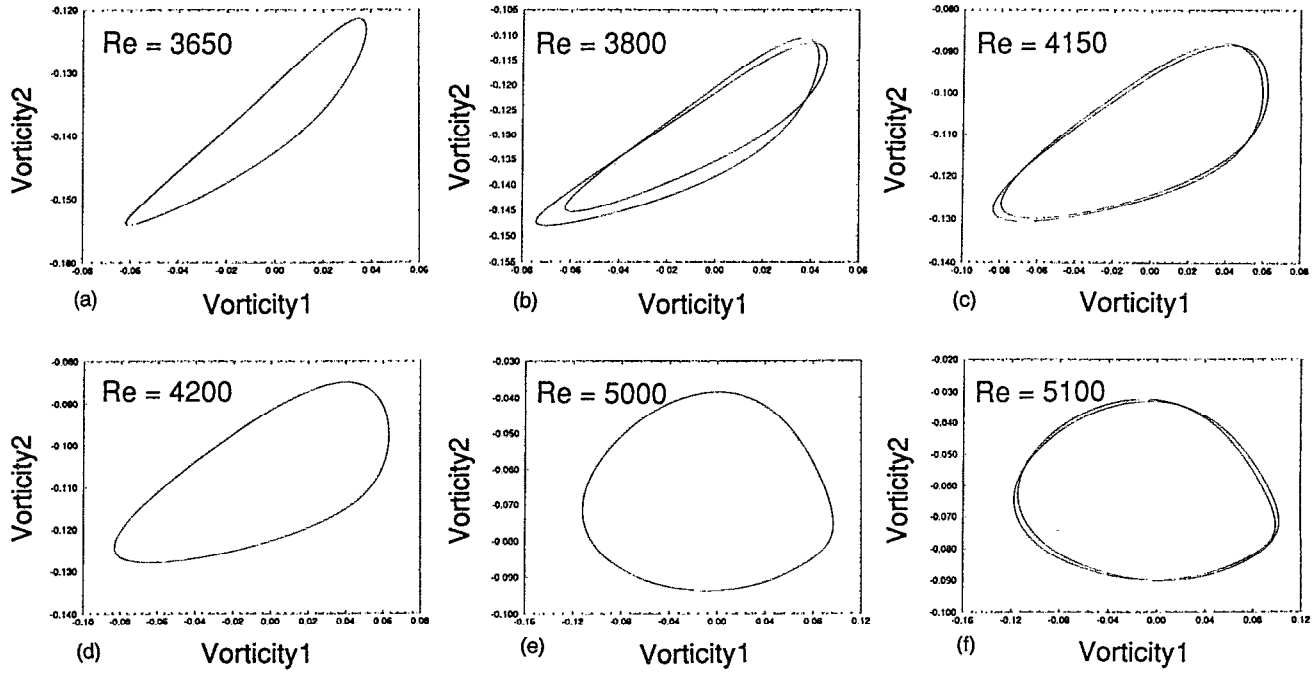

FIG. 14. (a)–(f) Branch of hysteresis by phase portraits.

to the basic frequency observed in front of the onset point at Re=6939, but corresponds apparently to the frequency appearing at Re=6000, i.e. $f=1/6f^{III}$. This phenomenon will be discussed later in the paper. The solutions turn periodic again by a second Ruelle-Takens scenario at Re=7500 to Re=7520, and a last inverse period doubling was observed from $f=2/6f^{III}=0.104$ at Re=7600 to $f=4/6f^{III}=0.212$ at Re=7750. The simulation was limited by Re=8000, thus no further transitions were observed. In Figs. 15(a)–15(i) successive domains of phase portraits from the branch of onset have been displayed.

The routes of the transition scenario: To summarize the basic features of the calculated transition scenario, we here give a short description of how the various branches are attained by continuously increasing or decreasing the Reynolds number. The *route of increasing Re*, or the "branch" observed by increasing the Reynolds number, starts from a stationary solution at Re=500, and follows the *branch of early transition* through a Hopf-bifurcation at Re=2500–2550, where the first fundamental frequency, $f^I=0.238$, sets in, to end at the periodic solution at Re=4000, where $f^I=0.246$. At Re=4000–4050 the branch is left by a jump of hysteresis to the *branch of hysteresis* with $1/2f^{III}=0.152$. Following this branch, to go to $1/2f^{III}=0.153$ at Re=5100 three doublings are passed, and the *branch of onset* is entered by a final jump of hysteresis.

The *route of decreasing Re*, or the "branch" observed by decreasing the Reynolds number, starts on the *branch of onset*. Proceeding, this is followed to a frequency $1/2f^{III}=0.152$ at Re=4750. At about Re=4725 the solution jumps by hysteresis to the *branch of hysteresis*, $f^{III}=0.307$ at Re=4500. This branch is followed through several bifurcations to end up with $f^{III}=0.303$ at Re=3650. Then the periodic solution jumps to the *branch through hysteresis*, $1/2f^{III}=0.168$ at Re=3600. Decreasing further, the branch is followed to the end where the solution jumps from $1/2f^{III}=0.167$ at Re=3300 to $f^I=0.242$ at Re=3200, which is located on the *branch of early transition*.

It may be noted that not all possible solutions are attainable by a monotone variation of the Reynolds number, e.g. to enter the upper part of the *branch through hysteresis* it is necessary to change the Reynolds number in both directions.

Onset to chaotic domain, Re=6939: By onset to chaotic domain we refer to the transition from periodic to aperiodic solutions. As expected from the Ruelle-Takens scenario a distinct spectral component appears in the broadband power spectrum when the behavior turns chaotic. This component, however, is not identical to the one observed just in front of the chaotic domain. To study in details this phenomenon, the critical onset number was as a first task localized by bisection to $\mathrm{Re}_{onset}=6939$. Thus, at Re=6935 and Re=6937 transients are attracted to a periodic solution, whereas they are expelled at Re=6939. The onset process was analyzed by simulating the transient behavior at the critical Reynolds number, $\mathrm{Re}_{onset}=6939$, starting from an initial periodic solution at Re=6930, see Fig. 15(i). Assuming the onset to the chaotic domain to be a penetrating bifurcation, the periodic branch may still exist, although it is unstable in the chaotic domain. Under such an assumption the stable periodic solution at Re=6930 may approximate the unstable periodic solution at Re=6939 very accurately. The destabilization process was then studied in time, applying phase portraits, Poincaré sections, and the correlation dimension based on 40,000 time steps. A first outcome is presented by the phase portraits in Figs. 16(a)–16(f), where N represents a sample containing 10,000 time steps. With a time

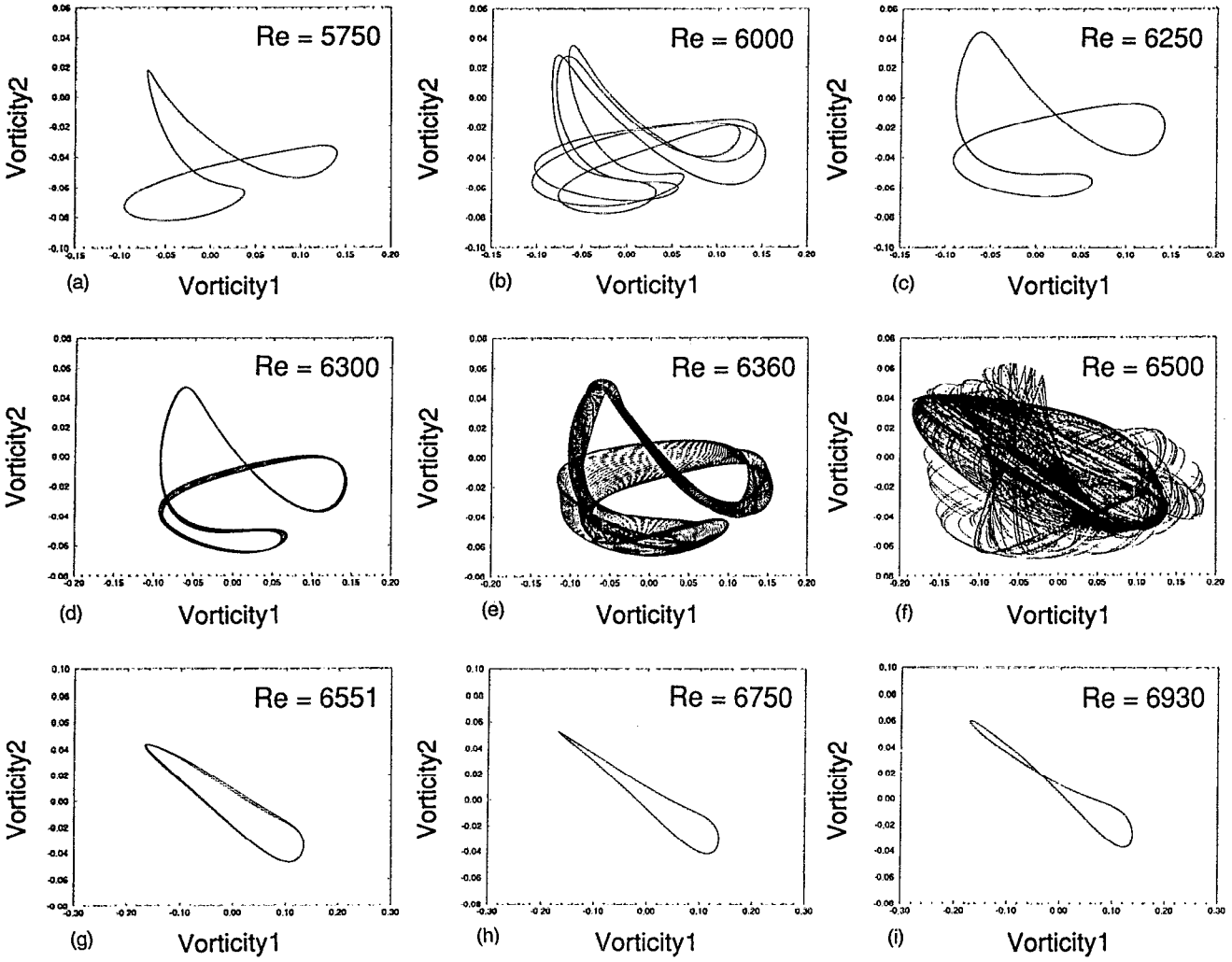

FIG. 15. (a)–(i) Branch of onset by phase portraits.

increment $\Delta t=0.05$, the Nth sample contains the time history from $t=500\cdot N$ to $t=500\cdot(N+1)$ which, with a lid period $T_{lid}=2\pi$, corresponds to about 80 revolutions of the lid. Starting by changing Re instantaneously from 6930 to 6939, the transients vary only slightly up to $N=100$, which corresponds to 10^6 time steps. At $N=140-142$ [Fig. 16(c)] a torus is observed to appear. This expands continuously up to $N=150-152$, Fig. 16(d). From hereon a dramatic expansion sets in and the final destabilization process occurs within further 10 sample intervals, Fig. 16(e). Hereafter the surface of the torus gets distorted and the solution turns chaotic. The onset process is most clearly demonstrated by taking the sum of vort1,...,vort5 and representing the difference between the maximum and minimum value of this, as function of the time intervals. In Fig. 17 this is denoted as amplitude of time series. This figure confirms the assumption of a penetrating bifurcation, proved by the long-winded growth of the amplitude. It is noticeable that the decisive collapse happens almost exactly at $N=167$. The peak at $N=178$ indicates the existence of an underlying structure, which is comparable to the phase portrait in Fig. 16 for $N=160-162$.

To clarify the destabilization process more precisely, the phase portraits were supplemented with Poincaré sections containing all the intersections points from $N=1$ to $N=194$ on some hypersurface, see Figs. 18(a)–18(d). In Figs. 18(a)–18(c) we have zoomed-in on a part of the Poincaré sections, with the frame of zooming marked by rectangular boxes. We here see that, coming from the periodic solution, the transients seem to be influenced by two frequencies, resulting in a surface modulation of the Poincaré sections, Fig. 18(d). After a certain time, $N=40$, the transients reorganize on a closed orbit, that is a torus in phase space, and from hereon the process proceeds in radial directions, as seen in Fig. 18(c). This continues up to $N=167$, where the attractor destabilizes and becomes strange. Measured by the correlation dimension,[32] ν_{corr}, the attractor increases from being one-dimensional at the initial state at Re=6930, to become two-dimensional up to $N=150$, to finally attain a fractal dimension of $\nu_{corr}=3.2$ for $N>167$, and thus becoming a non-random strange attractor. Corresponding Fourier transforms of transient time series show an initial frequency, say f_1, with a second frequency $2f_2$ appearing for $N<150$. In the Fourier spectra this is manifested

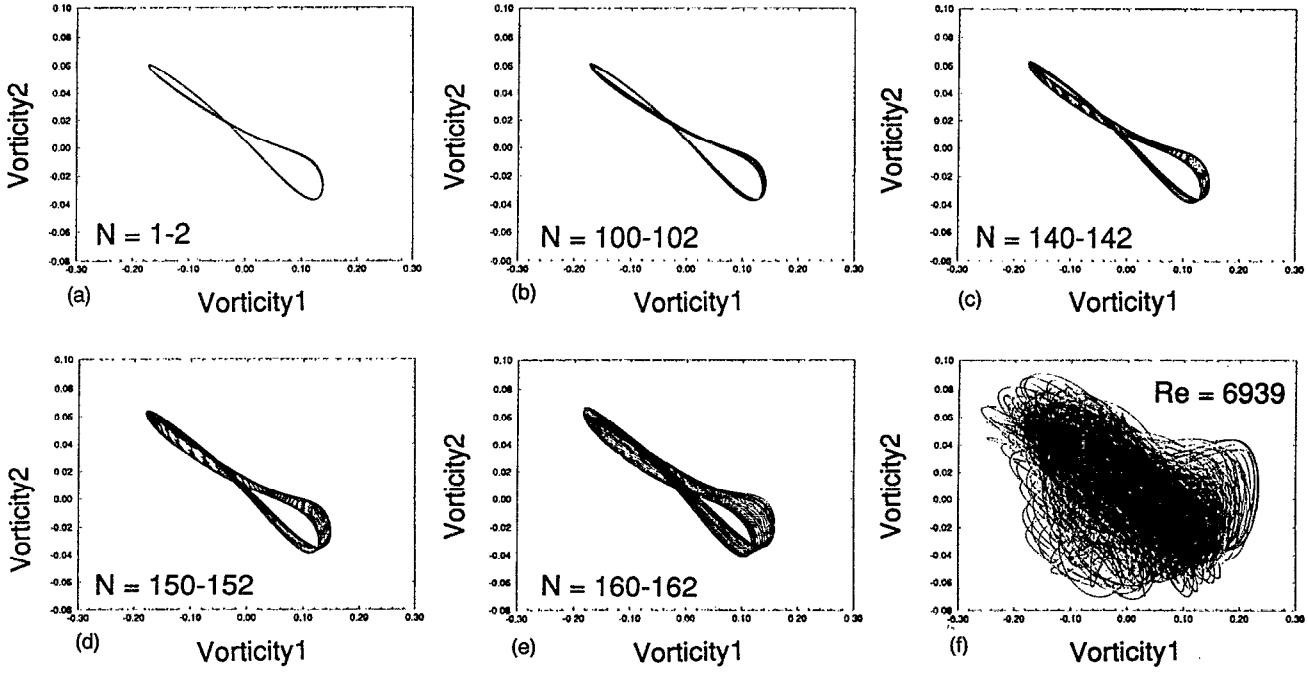

FIG. 16. (a)–(f) Onset process to a chaotic attractor.

by a strong component, $2f_2$, with accompanying harmonics $nf_1 \pm 2f_2$, which most significantly is observed for $N=51-62$, i.e. on the unstable torus. At $N=101-112$ energy is transferred to the harmonics, whereas for $N=151-162$ this pattern breaks, and f_2 is obtained. For $N>167$ the Fourier spectrum becomes broadbanded, and f_1 disappears whereas f_2 is preserved as the final spectral component.

The onset might be understood as a periodic bifurcation consisting of two simultaneous "Hopf-bifurcations" leading to strange attractor motion. The bifurcations destabilize the periodic solution and the transients converge to an unstable and transient torus at about $N=30$. The second frequency further destabilizes the torus, and causes the attractor to be strange as observed in the Ruelle-Takens scenario. In Fig. 19 the onset scenario is illustrated on diagram form.

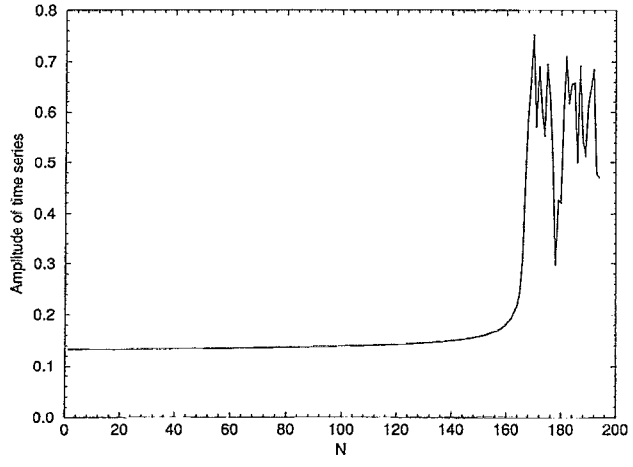

FIG. 17. The expansion of onset in time.

The spectral component is observed to bifurcate by an inverse period doubling from $f=1/6f^{III}=0.0518$ at $\mathrm{Re}=7250$ to $f=2/6f^{III}=0.104$ at $\mathrm{Re}=7500$, to end by a second Ruelle-Takens scenario. The "bifurcation" of the underlying structure in the strange attractor area has to our knowledge not been observed before, at least not as explicitly. The R-T frequencies were identified by very carefully studying the most energetic components, and the estimates were controlled for several times. This most surprisingly manifests an inverse period doubling between 7250 and 7500, and thus explains the appearance of a second component, and in fact completes the branch of onset by an underlying structure in the chaotic region, connected through an unstable torus of onset.

V. CONCLUSION

In the paper we have presented the flow structures and the numerical transition scenario of a rotating fluid flow in a closed cylinder, where the motion is created by a rotating lid. The numerical algorithm applied is confined to axial symmetry and has been validated against experimental visualizations of both transient and stable periodic flow in the early part of the transition process. The flow structures, constructed by numerically inserting particles into the flow and following these in time, show an astonishing agreement with experimental visualizations obtained by illuminating pollen particles by a laser sheet. The vortex dynamics, observed as stretching, folding and squeezing of structures about a central vortex core, were reproduced with high accuracy. Thus it is believed that the numerical algorithm represents the full dynamical flow scenario well into the unsteady domain. At

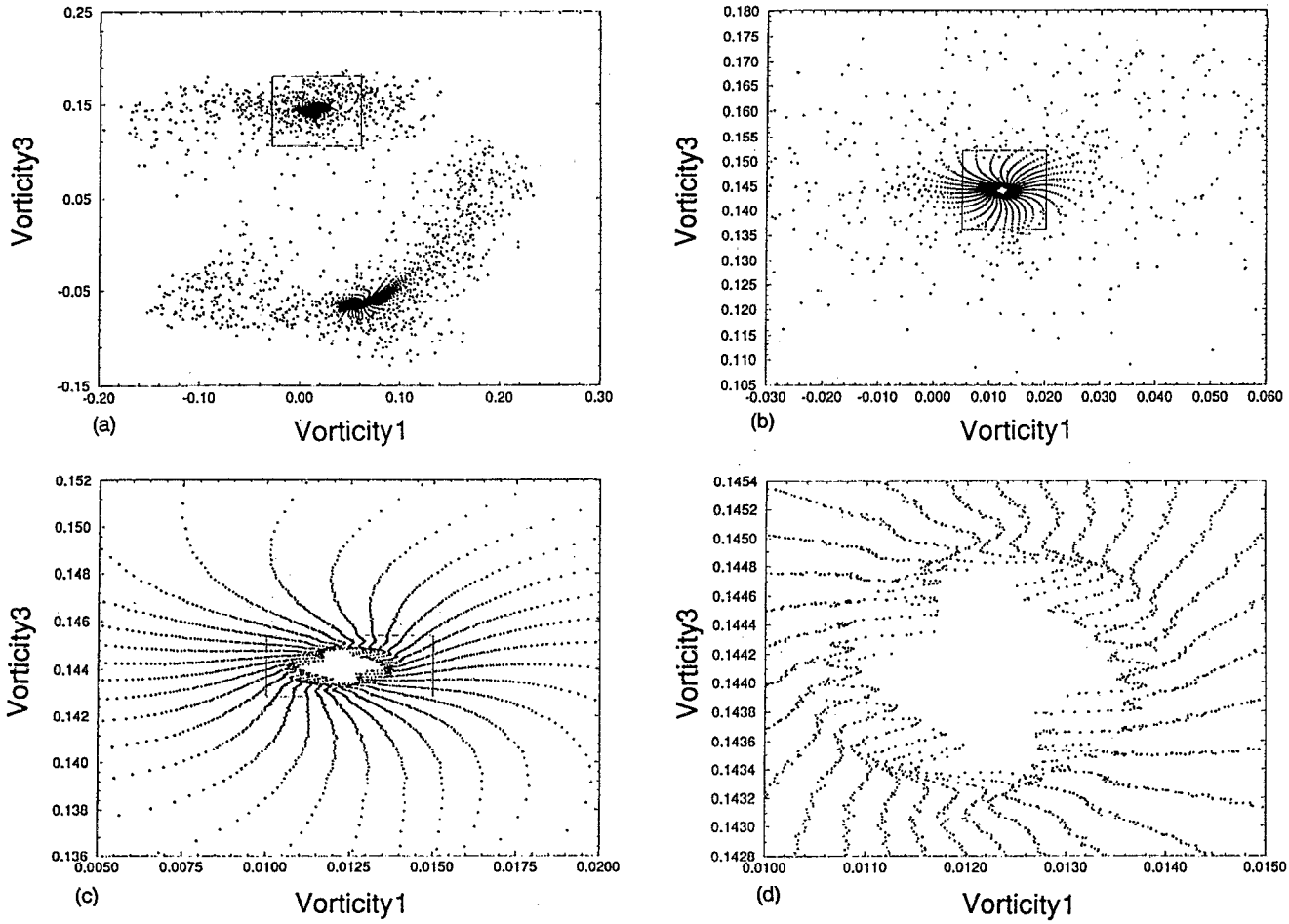

FIG. 18. (a)–(d) Poincare sections showing the onset process by successive expansions of scale.

higher Reynolds numbers (Re≥3500) three-dimensional effects have been observed in experiments and, as a consequence, the axisymmetric transition scenario becomes nonphysical from a certain symmetry breakdown number. The numerical algorithm, however, still satisfies the axisymmetric Navier-Stokes equations and therefore is assumed to represent basic features for a wider range of Re.

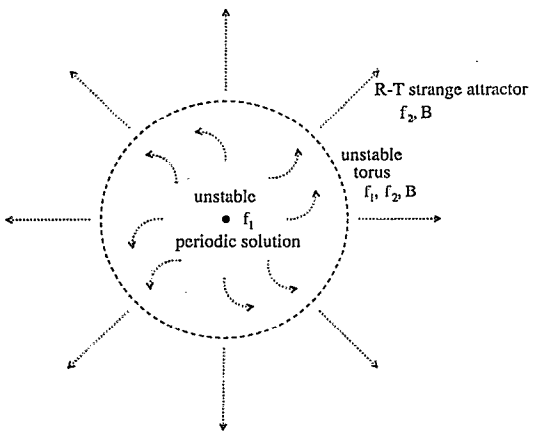

FIG. 19. Diagram of onset.

The direct numerical simulations were carried out with the aspect ratio fixed at $\lambda = 2$ and the Reynold number varied systematically in the range from 500 to 8000. A main outcome has been the resulting frequency diagram, shown in Fig. 9, which could be successfully related to bifurcation theory. Thus, by simple rules, outlined in Table I, it was possible to understand all fundamental transitions observed. The numerical simulations showed the existence of multiple solutions located on four discernible branches on the frequency diagram. The definition of a branch as the continuum of continuous deformations or bifurcations of stable solutions, gave constructive information of the transition scenario. Note that all branches were ended by jumps of hysteresis of which six were observed. The branches were illustrated by phase portraits in order to explain their basic nature in the phase space. A useful feature from the bifurcation theory is that the time of convergency is directly connected to the rate of attraction and thus to the stability of the solutions. Therefore, since two of the branches were left by very low-attractive endpoints we conclude them to be connected by an unstable branch of hysteresis through saddle-

node bifurcation points. The branches were found to possess three fundamental frequencies, f^I,f^{II} and f^{III}. Assuming the onset to chaos to be a penetrating bifurcation the process was simulated and the transition identified as a non-trivial Ruelle-Takens scenario through an unstable torus. The R-T frequency obtained was observed to be connected to the final spectral component by an inverse period doubling in the chaotic domain. Note that a lack in numerical resolution for the highest Reynolds numbers resulted in the chaotic domain being ended non-physically, but typically, by an area of periodic solutions. The full transition scenario is summarized in Table II.

ACKNOWLEDGMENTS

One of the authors (EAC) acknowledges financial support from the Danish Technical Research Council (Grant No. 16-4967-2 OS). The computer simulations, performed on the Amdahl VP1200 vector processor, was financed by the Danish Technical Research Council. P.L. Christiansen, P.S. Larsen, M. Brøns and O. Skovgaard are thanked for helpful support and advice during this project.

[1]D. Ruelle and F. Takens, "On the nature of turbulence," Commun. Math. Phys. **20**, 167 (1971).
[2]S. Newhouse, D. Ruelle, and F. Takens, "Occurrence of strange axiom A attractors near quasi periodic flows on T^m, $m \geq 3$," Commun. Math. Phys. **64**, 35 (1978).
[3]M. J. Feigenbaum, "Quantitative universality for a class of nonlinear transformations," J. Stat. Phys. **19**, 25 (1978).
[4]Y. Pomeau and P. Manneville, "Intermittent transition to turbulence in dissipative systems," Commun. Math. Phys. **74**, 189 (1980).
[5]S. Ostlund, R. D. J. Sethna, and E. Siggia, "Universal properties of the transition from quasi-periodicity to chaos in dissipative systems," Physica **8D**, 303 (1983).
[6]E. N. Lorenz, "Deterministic nonperiodic flow," J. Atmos. Sci. **20**, 130 (1963).
[7]J. P. Gollub and S. V. Benson, "Many routes to turbulent convection," J. Fluid Mech. **100**, 449 (1980).
[8]H. Schlichting, *Boundary Layer Theory*, Series in Mechanical Engineering, 7th Ed. (McGraw-Hill, New York, 1979).
[9]H. J. Lugt, *Vortex Flow in Nature and Technology* (Wiley, New York, 1983).
[10]U. T. Bödewardt, "Die drehstömung über festem grunde," Z. Angew. Math. Mech. **20**, 241 (1940).
[11]H. U. Vogel, "Experimentelle ergebnisse über die laminare strömung in einem zylindrischen gehaüse mit darin rotierender scheibe," Bericht 6, Max-Planck-Institut für Strömungsforschung, Gottingen, 1968.
[12]B. Ronnenberg, "Ein selbstjustierendes 3-komponenten-LDA nach dem vergleichstrahlverfahren, angewendt für untersuchungen in einer stationaren zylindersymmetrischen drehströhmung mit einem rückströmgebiet," Bericht 20, Max-Planck-Institut für Strömungsforshung, 1977.
[13]M. P. Escudier, "Observations of the flow produced in a cylindrical container by a rotating endwall," Exp. Fluids **2**, 189 (1984).
[14]J. A. Michelsen, "Modeling of laminar incompressible rotating fluid flow," Report No. AFM 86-05, Department of Fluid Mechanics, Technical University of Denmark, 1986.
[15]C. Westergaard, P. Buchhave, and J. Sørensen, "PIV measurements of turbulent and chaotic structures in a rotating flow using an optical correlator," in *Laser Techniques and Applications in Fluid Mechanics*, edited by R. J. Adrian (Springer-Verlag, Berlin, 1993), pp. 243–265.
[16]J. N. Sørensen, "Visualizations of rotating fluid flow in a closed cylinder," Report No. AFM 92-06, Department of Fluid Mechanics, Technical University of Denmark, 1992.
[17]A. Spohn, "Ecoulement et éclatement tourbillonnaires engendrés par un disque tournant dans une enceinte cylindrique," Ph.D. thesis, Université J. Fourier, Grenoble, 1991.
[18]H. P. Pao, "A numerical computation of a confined rotating flow," J. Appl. Mech. **37**, 480 (1970).
[19]M. Bertela and F. Gori, "Laminar flow in cylindrical container with a rotating cover," J. Fluids Eng. **104**, 31 (1982).
[20]H. J. Lugt and H. J. Haussling, "Axisymmetric vortex breakdown in rotating fluid within a container," J. Appl. Mech. **49**, 921 (1982).
[21]H. J. Lugt and M. Abboud, "Axisymmetric vortex breakdown with and without temperature effects in a container with rotating lid," J. Fluid Mech. **179**, 179 (1987).
[22]J. M. Lopez, "Axisymmetric vortex breakdown. Part 1. Confined swirling flow," J. Fluid Mech. **221**, 533 (1990).
[23]J. M. Lopez, "Axisymmetric vortex breakdown in an enclosed cylinder flow," Lect. Notes Phys. **323**, 385 (1989).
[24]J. M. Lopez and A. D. Perry, "Axisymmetric vortex breakdown. Part 3. Onset of periodic flow and chaotic advection," J. Fluid Mech. **234**, 449 (1992).
[25]O. Daube and J. N. Sørensen, "Simulation numérique de l'écoulement périodique axisymétrique dans une cavité cylindrique," C. R. Acad. Sci. Paris **308**, 463 (1989).
[26]E. A. Christensen, J. N. Sørensen, M. Brøns, and P. L. Christiansen, "Low dimensional representation of early transition in rotating fluid flow," Theoret. Comput. Fluid Dyn. **5**, 259 (1993).
[27]J. N. Sørensen and Ta Phouc Loc, "High-order axisymmetric Navier-Stokes code description and evaluation of boundary conditions," Int. J. Num. Methods Fluids **9**, 1517 (1989).
[28]E. L. Wachspress, *Iterative Solutions of Elliptic Systems* (Prentice-Hall, Englewood Cliffs, NJ, 1966).
[29]D. W. Peaceman and H. H. Rachford, "The numerical solution of parabolic and elliptic differential equations," J. Soc. Ind. Appl. Math. **3**, 28 (1955).
[30]J. Guckenheimer and P. Holmes, *Nonlinear Oscillations, Dynamical Systems, and Bifurcations of Vector Fields* (Springer-Verlag, Berlin, 1983), Vol. 42 of AMS.
[31]P. Huerre and P. A. Monkewitz, "Absolute and convective instabilities in free shear layers," J. Fluid Mech. **159**, 151 (1985).
[32]P. Grassberger and I. Procaccia, "Characterization of strange attractors," Phys. Rev. Lett. **50**, 346 (1983).
[33]J.-P. Eckmann and D. Ruelle, "Fundamental limitations for estimating dimension and Lyapunov exponents in dynamical systems," Physica D **56**, 185 (1992).
[34]D. D. Joseph, "Direct and repeated bifurcation into turbulence," in *Approximation Methods for Navier-Stokes Problems*, edited by A. Dold and B. Eckmann, Lecture Notes in Mathematics (Springer-Verlag, Berlin, 1979), Vol. 771, pp. 249–264.
[35]S. Wiggins, *Introduction to Applied Nonlinear Dynamical Systems and Chaos* (Springer-Verlag, Berlin, 1990), Vol. 2 of TAP.